Discover Oncology

Research

ZNF385A was identified as a novel colorectal cancer-related functional gene by analysis of the interaction and immune characteristics of oxidative stress and the inflammatory response

Yaqi Guo[2] · Shipeng Shang[3] · Leilei Liang[4] · Enrui Liu[1]

Received: 5 November 2024 / Accepted: 3 March 2025
Published online: 10 March 2025

Abstract

Background Recently, oxidative stress and inflammatory responses have been shown to directly impact tumor growth and the tumor microenvironment (TME). However, more research is necessary to fully understand the relationship between oxidative stress and inflammatory responses and colorectal cancer (CRC).

Methods The FindCluster algorithm was used to extract CRC Single-cell RNA sequencing (scRNA-seq) data and identify tumor cell groupings. From the MSigDB database, genes associated with oxidative stress and the inflammatory response were taken. We identified molecular subtypes and built a predictive risk model with the LASSO-Cox method using the ConsensusClusterPlus software suite. We incorporated the prognostic risk model and other clinicopathological parameters into a column-line chart. Finally, we used Quantitative Polymerase Chain Reaction (qPCR) and immunohistochemistry to check the expression of the unreported hub model genes. Cell proliferation was assessed using EDU and colony formation assays. Reactive Oxygen Species (ROS) tests were used to quantitatively determine the ROS content in CRC cells. The ability of CRC cells to invade and migrate was examined using transwell experiments. The regulatory functions of hub model genes were discovered in vivo using a xenograft model tumor assay.

Results Oxidative stress and inflammatory response factors in monocytic/macrophages of CRC were significantly upregulated, and their oxidative stress and inflammatory response functions were significantly higher than those of other cell subgroups, as indicated by the enrichment score. These factors showed significant synergistic overexpression and enrichment in this cell population. We constructed a prognostic risk model consisting of seven signatures. The good and stable prognostic evaluation efficacy of the model was confirmed, and risk scores were determined to be independent prognostic factors for CRC. We explored the relationship between the risk score model and malignant progression of tumor cells, tumor immune microenvironment, genomic variation, chemotherapy resistance, and immune response. Further qPCR and immunohistochemistry analysis showed that the expression of ZNF385A was high in CRC tissues. The functional experiment results indicated that interfering with the expression of ZNF385A could suppress the proliferation, ROS, migration and invasion of SW620 cells in vitro and the growth of xenograft tumors in vivo.

Conclusion In this study, we investigated the critical expression patterns of oxidative stress- and inflammatory response-related genes in CRC, which may contribute to the prognosis and immunotherapy of CRC. Additionally, we discovered

Supplementary Information The online version contains supplementary material available at https://doi.org/10.1007/s12672-025-02024-1.

✉ Enrui Liu, liuenrui1992@163.com | [1]Department of Emergency Surgery, The Affiliated Hospital of Qingdao University, Qingdao, Shandong, People's Republic of China. [2]Department of Anesthesiology, The Affiliated Hospital of Qingdao University, Qingdao, Shandong, People's Republic of China. [3]School of Basic Medicine, Qingdao University, Qingdao, Shandong, People's Republic of China. [4]National Cancer Center/National Clinical Research Center for Cancer/Cancer Hospital, Chinese Academy of Medical Sciences and Peking Union Medical College, Beijing 100021, China.

ZNF385A to be a novel oncogene in CRC. These findings imply that this model may be applied to assess prognostic risk and identify potential therapeutic targets for CRC patients.

1 Introduction

Colorectal cancer (CRC) is the third most common cancer and the second leading cause of cancer-related death worldwide [1, 2]. Despite the overall decline in incidence rate and mortality, there has been an exponential increase in the incidence rate of rectal cancer among individuals under 50 years old [3]. Moreover, the treatment of CRC patients is a complex process that involves decisions regarding surgery, preservation of intestinal function, restoration of normal anal control, and preservation of urinary and reproductive system function [4, 5]. For most patients with localized CRC, the current recommendation is to combine radiotherapy, chemotherapy, and surgery [6]. However, due to the complexity and poor prognosis of CRC, it is necessary to approach its mechanism and treatment from a new perspective.

Oxidative stress refers to an imbalance between oxidation and antioxidation in the body, which can lead to inflammation characterized by neutrophil infiltration, increased protease secretion, and the production of a large number of oxidation intermediates [7]. The inflammatory response is the body's defense mechanism used to detect and remove harmful foreign substances and initiate the self-healing process [8]. Oxidative stress and inflammation are closely related to cancer occurrence and development. The relationship between free radicals generated by oxidative stress and cancer is complex, and an excessive amount of free radicals can increase the risk of cancer. However, controlling the amount of free radicals in cells is crucial for the division and proliferation of cancer cells to prevent excessive DNA damage caused by free radicals, and genetic mutations promote the generation and replication of cancer cells. Before the formation of cancer cells, free radicals such as ROS are carcinogenic [9]. The inflammatory NF-κB transcription factor pathway is a key factor in cancer pathogenesis, and cellular inflammation provides a microenvironment for cancer cells [10]. Inflammation and oxidative stress interact, leading to increased ROS production, which exacerbates inflammation [11]. NLRP3 in the NADPH oxidase in immune cells is a "sensor" called the inflammatome that can sense PAMPs from bacteria and DAMPs from damaged cells and activate the NF-κB transcription factor pathway, producing a large number of inflammatory cytokines [12]. Severe oxidative stress can increase the expression of NLRP3, leading to the production of more inflammatory cytokines. The interaction between oxidative stress and inflammation jointly affects tumor cell occurrence and development [13]. Immune cells within the tumor microenvironment (TME) also play a critical role in tumorigenesis [14]. An increasing number of studies have shown that oxidative stress and inflammatory reactions are closely related to the immune microenvironment of tumors, with M2 macrophages, dendritic cells, and T cells being the main components of the immunosuppressive TME in ROS-induced inflammation [15]. Proinflammatory cytokines, including tumor necrosis factor α (TNFα), interleukin (IL)−1, IL-6, and certain chemokines, play an important role in CRC-related cachexia. Furthermore, the tumor microenvironment (TME) can lead to systemic inflammation, oxidative stress, and increased fibrosis [16].

The findings of this study have significant practical applications in colorectal cancer (CRC) management. The critical expression patterns of oxidative stress- and inflammatory response-related genes can aid in developing prognostic tools to stratify patient risk and personalize treatment strategies. Moreover, these patterns may serve as biomarkers to predict patient responses to immunotherapy, potentially enhancing the effectiveness of such treatments. The identification of ZNF385A as a novel oncogene opens new avenues for therapeutic targeting, with possibilities for drug development or genetic interventions to mitigate its oncogenic effects. Together, these insights provide a foundation for advancing precision medicine in CRC by improving prognosis assessment, optimizing immunotherapy, and identifying innovative therapeutic targets.

2 Methods

2.1 Download and preprocessing of data

Using the R program TCGAbiolinks, we retrieved the FPKM expression profiles and survival data for COAD and READ from the TCGA database. Additionally, using the mafs() function in the R package maftools for genomic variation analysis, we downloaded mutation data for the associated data and combined the maf files of two datasets.

We created a Seurat single-cell object as input for the single-cell dataset analysis and retrieved the expression file and meta-information file of CRC samples from the GSE139555 dataset in the GEO database.

We obtained the expression spectra and survival data of the GSE161158, GSE143985, and GSE92921 datasets from the GEO database for external validation of the risk model.

2.2 Identification and characterization of single-cell subpopulations

The single-cell dataset was examined using the specialist single-cell transcriptome analysis R software Seurat (http://satijalab.org/seurat/). To consolidate the data, we first chose the sequencing results of CRC samples from this single-cell dataset. Next, we used Seurat's CreateSeuratObject() function to create a Seurat object with a minimum of 5 cells and 500 features. We first filtered genes and cells, with the mitochondrial gene ratio set to less than 20%, the number of features set to 500–6000, and the number of counts set to 500–40000. When the percentage of reads from red blood cells fell below the 20% cut-off, cells were once more filtered. After data standardization, we ran ScaleData() once more and changed the hypervariable gene's value to 2000. After that, we used PCA to analyse the data in terms of dimensional reduction, and we used the ElbowPlot() function to calculate the principal component score for further study. After PCA, we utilized UMAP to further reduce the dimensionality of the data and found tumor cell subgroups using FindClusters(). Using MonoImmunoData as the cell type reference database, we used the R package SingleR (https://github.com/SingleR-inc/SingleR) to annotate the clustering findings depending on a certain resolution. The criteria were set to avg_log2FC > 0.5 and p_val_adj 0.05 to screen markers in subgroups. All marker genes in all subgroups were identified using the FindAllMarkers() method with min.pct = 0.25 and logfc.threshold = 0.25. We conducted a differential expression study between two cell populations using the method FindMarkers(), setting the threshold to |avg_Log2FC| > 0.5 and p_val_adj 0.05 for differentially expressed genes between the two. To visualize the distribution of active cell populations and the results of dimensionality reduction in the single-cell expression data, we utilized the DimPlot() function. Gene expression was shown using the DotPlot() and FeaturePlot() functions, while cell type percentage analysis and gene expression visualization were performed using the R package plot1 cell.

2.3 Construction of prognostic risk model

To find tumor prognostication-related genes with subtype differences ($p < 0.01$), we first performed single-factor Cox analysis. Next, we built a prognostic risk score model for CRC based on these genes. To decrease the number of genes in the risk model, we screened variables using the Lasso approach. Finally, we used a multivariate Cox regression model to build a colorectal cancer risk score model. The calculation formula is as follows:

$$\text{Riskscore} = \sum_{i=0}^{n} \beta i * \chi i$$

Bi is the weight coefficient of each gene; χi is the expression amount of each gene.

We created ROC (receiver operating characteristic) curves using the R package timeROC to assess the perturbation scoring model's ability to predict outcomes. Additionally, we produced a scatter plot of the sample scores as well as a scatter plot of the survival time and status using ggplot2. Using the median risk score as the cut-off, we classified the tumor samples into high- and low-risk categories. To create survival curves for prognostic analysis, the Kaplan—Meier method was utilized, and a log-rank test was used to assess whether differences were significant.

2.4 Estimation of the proportion of immune infiltrating cells and immune score

We calculated the percentage of immune infiltrating cells using the TCGA CRC dataset expression profile and the CIBERSORT, ESTIMATE, xCell, and ssGSEA algorithms from the R package IOBR [17]. Based on gene expression profiles in complex tissues, the CIBERSORT algorithm is a technique for assessing cell composition. The tumor's immunological score, tumor purity, matrix score, and ESTIMATE score were all determined using the ESTIMATE algorithm. Based on 64 immune cell and stromal cell types' gene expression data, xCell can perform cell type enrichment analysis.

2.5 Drug sensitivity analysis

To forecast the sensitivity (IC50 value) of 138 medicines in the GDSC database, we used gene expression data from the TCGA CRC cohort with the R tool pRRophic (https://github.com/paulgeeleher/pRRophetic2).

2.6 Tissue specimens

Fresh CRC tissues and adjacent normal tissues were collected from the Affiliated Hospital of Qingdao University. No patients received treatment before surgery. The study was approved by the Ethics Committee of the Affiliated Hospital of Qingdao University.

2.7 Cell culture and transfection

The American Type Culture Collection contributed the human CRC cell line SW620. The cell lines were grown in 1640 medium supplemented with 10% FBS (Invitrogen, San Diego, CA) in a humid incubator at 37 °C with 5% CO_2.

Genepharma (Shanghai, China) provided the control sequences (si-NC) and interference sequences (si-ZNF385A) that were used to create ZNF385A-interfering SW620 cell lines. Using Lipofectamine 2000 (12566014, Invitrogen, Shanghai, China), cells were transfected with interfering expression in accordance with the manufacturer's instructions.

2.8 Quantitative real-time PCR and immunohistochemistry analysis

RNA extraction and quantitative real-time PCR (qRTPCR) analysis were performed using RNA-easy Isolation Reagent (No. RC112-01, Vazyme, China), a HiScript III 1st Strand cDNA Synthesis Kit (No. R312-01, Vazyme, China) and ChamQTM Universal SYBR® qPCR Master Mix (No. Q712-02, Vazyme, China) according to the manufacturer's instructions. The primer sequences were as follows: MPZ Forward Sequence 5′–3′: GTCAACTCGGAGGTCCAACTGA and Reverse Sequence 5′–3′: TCTTGTGACGGCTCAGTAGTGG; GAPDH Forward Sequence 5′–3′: GTCTCCTCTGACTTCAACAGCG and Reverse Sequence 5′–3′: ACCACCCTGTTGCTGTAGCCA. GAPDH served as an internal control.

An immunohistochemistry (IHC) staining SP kit (No. SP-9000, ZSGB-BIO, Beijing, China) was used for IHC, and anti-ZNF385A (LS-B8062, LS Bio, Beijing, China) (1:200) was purchased from LS Bio. The magnification of the IHC images was 20×.

2.9 Measurement of intracellular ROS levels

The levels of intracellular ROS were determined by a Reactive Oxygen Species Assay Kit (Beyotime Biotechnology, China). Briefly, after the indicated treatments, the cells were washed twice with PBS and incubated with 5 μM DCF-DA for 30 min at 37 °C in the dark. Equal amounts of cells were washed and subsequently suspended in culture medium for microplate reader analysis. Green fluorescence intensity was positively correlated with the level of ROS.

2.10 Colony formation assay

At 10^3 cells per plate, cells were seeded into 6-well plates. The cells were combined and then cultivated in culture media with 10% FBS and 1640 for 7 days. The following criterion was taken into account when assessing the outcomes: Colonies were defined as collections of 30 cells or more.

2.11 Cell migration and invasion assays

For the migration assay, 1.5×10^5 cells were placed in the upper chamber of a Transwell plate (Corning, NY, USA), and 700 μl of DMEM containing 20% serum was added to the lower chamber. The Transwell chamber was removed after being incubated for 24 h at 37 °C, cleaned once with PBS, flushed, and stained with 0.5% crystal violet. Using ImageJ, the relative cell density was calculated. The mean and SD from three different experiments were used to show the findings.

2.12 Xenograft model tumor assay

The Affiliated Hospital of Qingdao University gave its approval to the animal trials. CRC cells (2 × 106) were subcutaneously implanted into 4- to 6-week-old naked mice. The formula used to determine the tumor volume (V) is $V = 0.524 \times LW^2$, where L and W represent the tumor's length and width, respectively. The xenograft tumors were removed and weighed at the conclusion of the experiment, after which the mice were euthanized by an intraperitoneal injection of 100 mg/kg pentobarbital sodium (Sigma, St. Louis, MO, USA).

2.13 Statistical analysis description

In the statistical analysis, we compared differences between two groups of samples using the Wilcoxon test and between numerous groups of samples using the Kruskal—Wallis test. The following symbols were used to indicate statistical significance: ns for $p > 0.05$, * for $p \le 0.05$, ** for $p \le 0.01$, *** for $p \le 0.001$, and **** for $p \le 0.0001$.

3 Results

3.1 Dysregulation of oxidative stress and inflammatory response in tumor tissue

We collected a total of 10,119 cells from CRC tumor tissue and normal tissue after quality assurance and screening (Fig. 1). We chose the top 15 main components for further dimensionality reduction and analysis after performing an initial data dimensionality reduction analysis (PCA). Figure 2A displays these findings and lists a total of 11 distinct cell types, including two significant cell populations made up of stromal and immune cells, with annotation outcomes that are in line with the data from the original dataset. To examine variations in cell type distribution across various tissues, we created a proportionate distribution map of cell types. In contrast to immunological T cells, myofibroblasts, and other cells, NK cells were more widely distributed in normal tissues than in tumor tissues (Fig. 2B). The ssGSEA method was then used to calculate the oxidative stress and inflammatory response scores of each cell, and a violin plot was used to examine functional differences. The findings demonstrated that tumor tissue cells had much greater levels of oxidative stress and

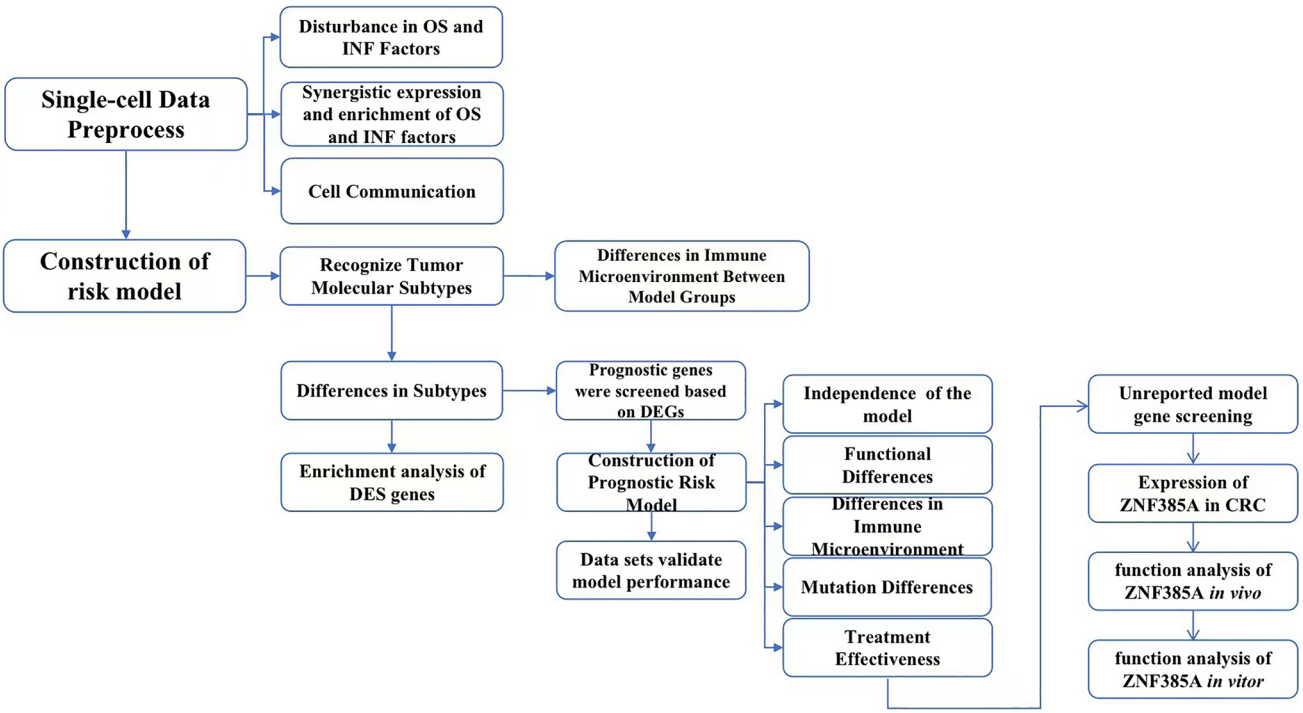

Fig. 1 Flow chart of the research design and data processing

inflammatory response than normal cells (Fig. 2C). We performed differential expression analysis on cells and discovered 136 genes that were significantly differentially expressed, including 11 genes associated with oxidative stress and 8 genes connected to the inflammatory response. These differentially expressed genes were most prominently abundant in monocytes and macrophages and highly expressed in tumor tissue, according to expression bubble plots (Figs. 2D and E).

3.2 Coexpression and enrichment of oxidative stress and inflammatory response

We initially identified marker genes for each cell subgroup in CRC and then chose functional-specific marker genes to map their expression profiles to analyse the heterogeneity of each cell population. The expression bubble plot of particular oxidative stress marker genes is shown in Fig. 3A (Table S1). Myofibroblasts, mast cells, and monocytes/macrophages express more oxidative stress-related molecules, particularly monocytes/macrophages. Inflammatory response-associated marker genes (Table S2) were substantially expressed in monocytes and macrophages, as shown in Fig. 3B. We used a violin plot (Fig. 3C and D) to compare variations in oxidative stress and inflammatory response among diverse cell groups. It is clear that oxidative stress and the inflammatory response have the highest scores in monocytes and macrophages.

When we compared the ssGSEA scores of the two gene sets in monocytes and macrophages, we discovered a strong positive association between oxidative stress and the inflammatory response (Spearman correlation coefficient = 0.25; Fig. 3E). To do this, we performed KEGG pathway and Gene Ontology Biological Process (GOBP) functional enrichment studies on monocyte and macrophage marker genes. The KEGG analysis of the marker gene enrichment revealed that it was primarily enriched in pathways related to lysosomes, bacteriophages, bacterial infections, osteoclast development, and antigen processing and presentation (Fig. 3F). According to the GOBP findings, the marker gene was primarily enriched in myeloid leukocyte activation, immune response regulation, responses to lipopolysaccharides and molecules derived from bacteria, antigen processing and presentation, positive regulation of cell activation, positive regulation of external stimuli, and cell activation involved in immune responses (Fig. 3G).

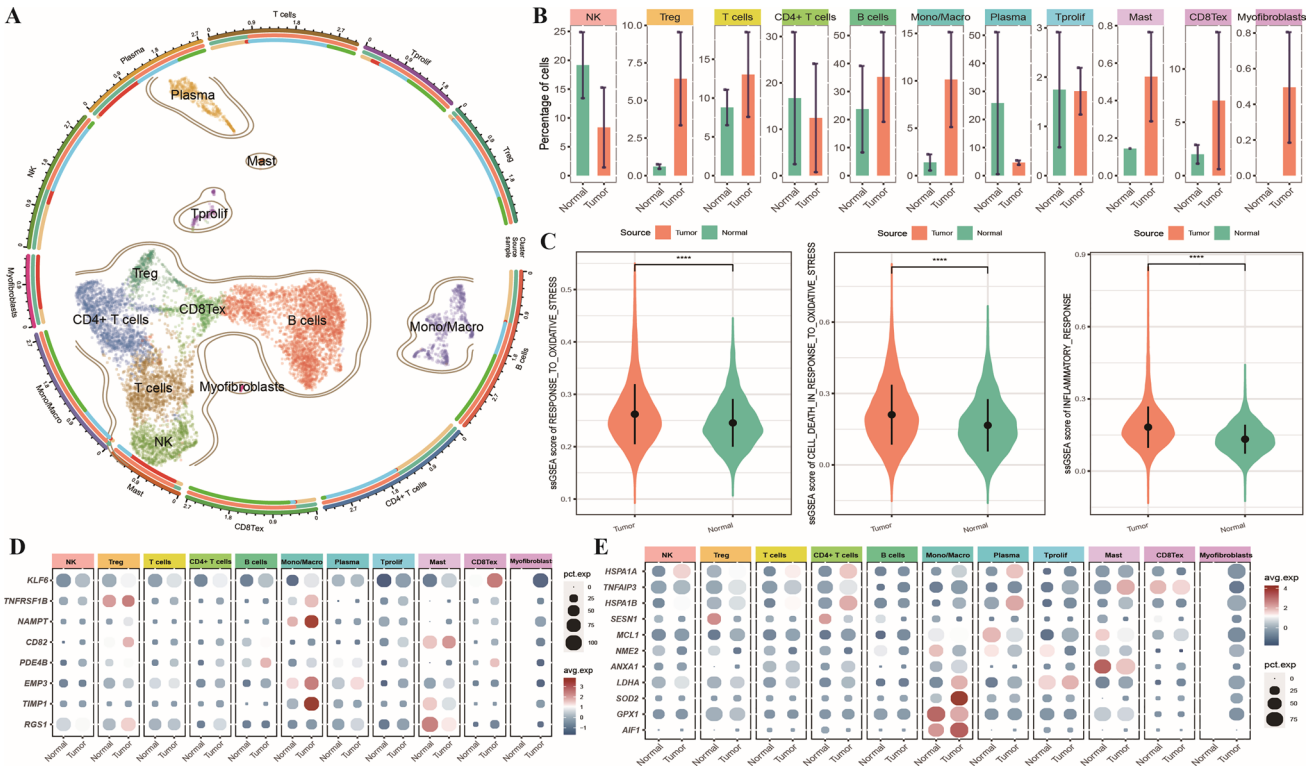

Fig. 2 **A** A total of 11 distinct cell types, including two significant cell populations made up of stromal and immune cells, with annotation outcomes that are in line with the data from the original dataset; **B** In contrast to immunological T cells, myofibroblasts, and other cells, NK cells were more widely distributed in normal tissues than in tumor tissues; **C** tumor tissue cells had much greater levels of oxidative stress and inflammatory response than did normal cells; **D**, **E** 11 genes associated with oxidative stress and 8 genes connected to the inflammatory response

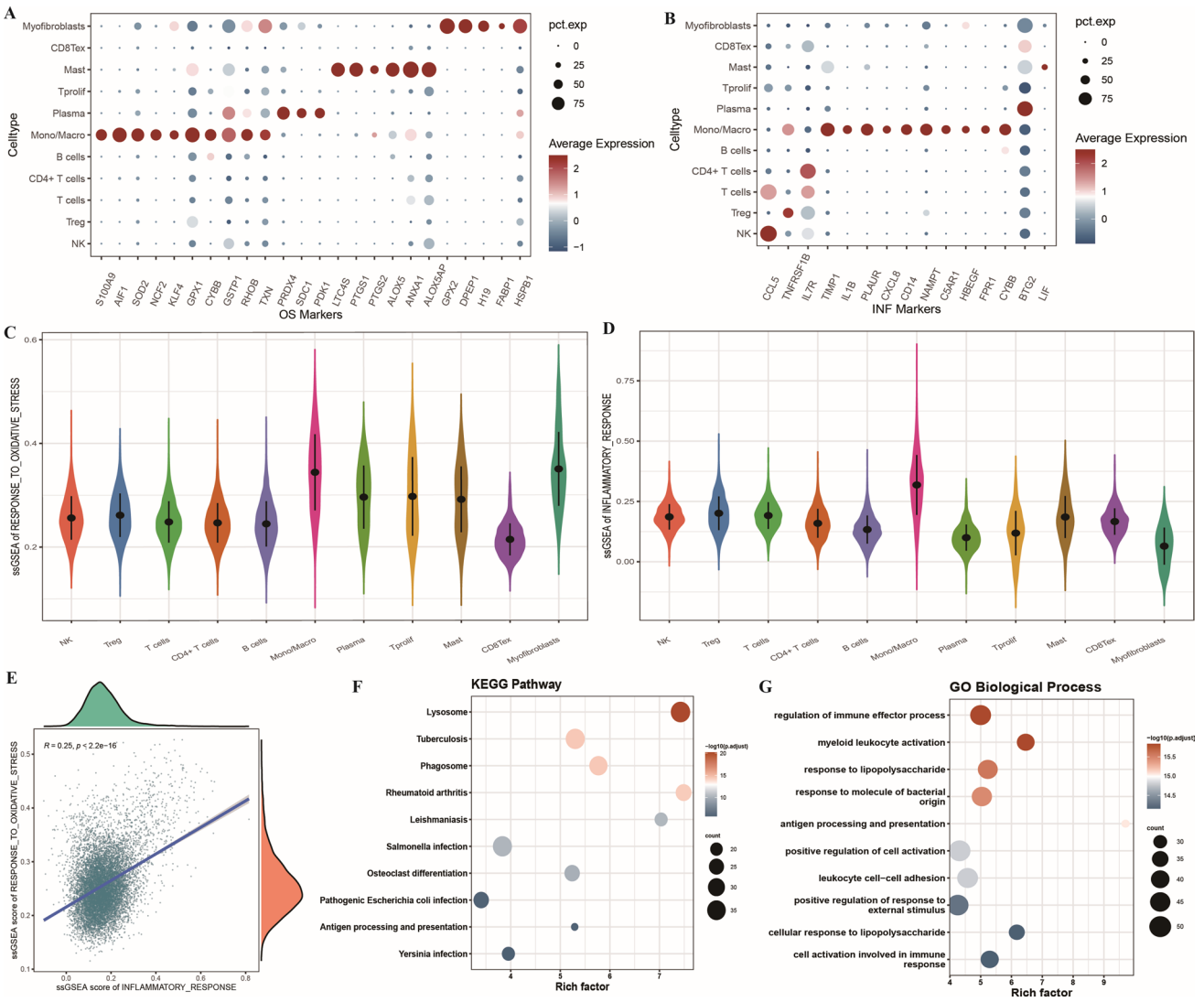

Fig. 3 **A** The expression bubble plot of particular oxidative stress marker genes; **B** Inflammatory response-associated marker genes are substantially expressed in monocytes and macrophages. **C**, **D** oxidative stress and inflammatory response have the highest scores in monocytes and macrophages; **E** a strong positive association between oxidative stress and inflammatory response; **F** it was primarily enriched in pathways related to lysosomes, bacteriophages, bacterial infections, osteoclast development, and antigen processing and presentation. **G** the marker gene was primarily enriched in myeloid leukocyte activation, immune response regulation, responses to lipopolysaccharides and molecules derived from bacteria, antigen processing and presentation, positive regulation of cell activation, positive regulation of external stimuli, and cell activation involved in immune responses

3.3 Cell communication

Then, using the single-cell dataset's annotation findings and expression data, we described cellular communication in CRC. The findings examined the cellular communication between B cells and other cells and demonstrated that B cells communicate with other cells in the carcinogenesis of CRC (Fig. 4A). Figure 4B displays a network diagram of the oxidative stress-related gene APP signaling pathway, one of the signaling pathways of the cellular communication network, in which myofibroblasts communicate by sending and receiving signals from various cell populations. Figures 4C and D show the signalling pathway network diagram of the inflammatory response-related genes CD40 and LCK. LCK is a signaling pathway for interactions between different T-cell populations, whereas CD40 is a signaling pathway for interactions between B cells and CD4+ T cells. Monocytes and macrophages are the primary signal emitters in the ICAM, CD86 (Fig. 4F, G) and MHC-II signaling pathways, whereas CD8Tex cells and Treg cells are the primary signal recipients

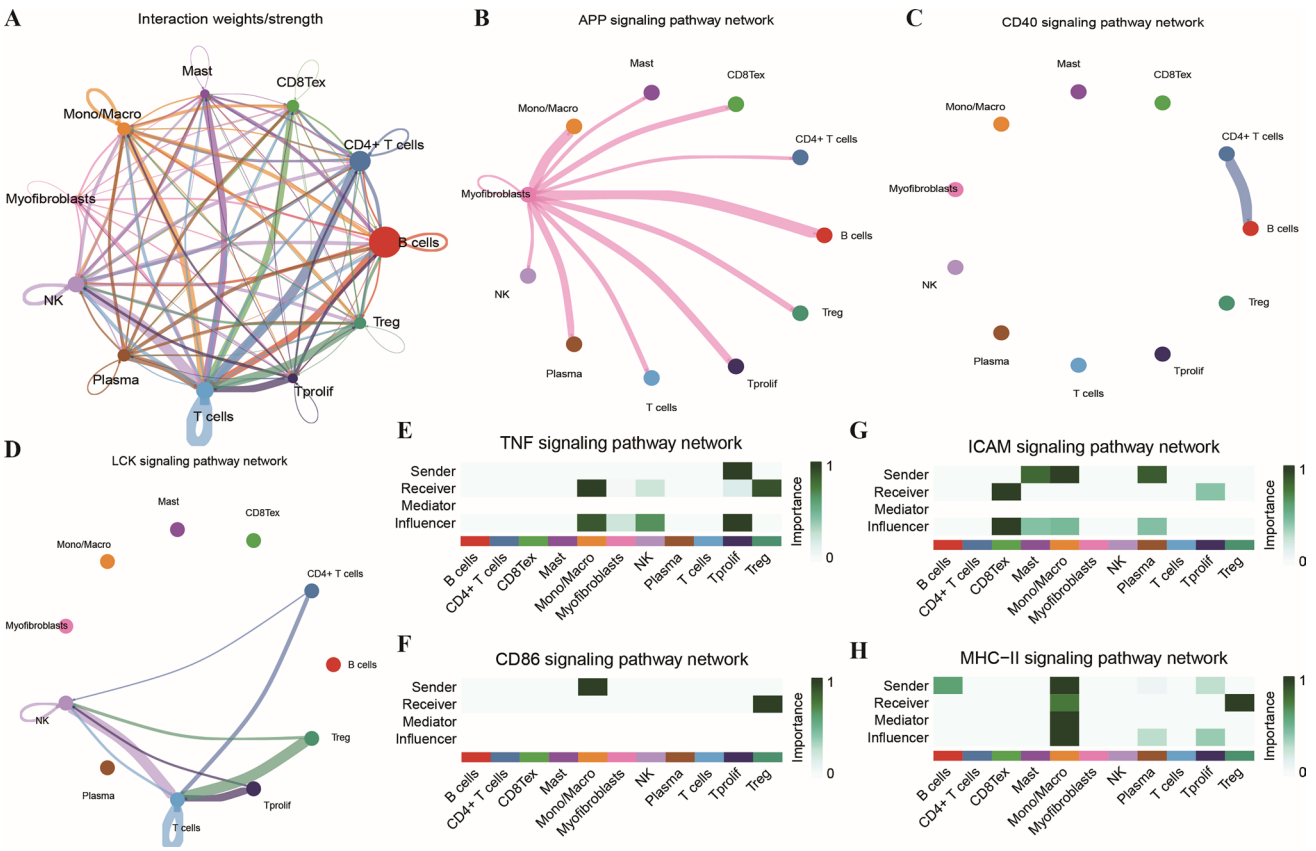

Fig. 4 **A** The findings examined the cellular communication between B cells and other cells and demonstrated that B cells play a significant role in the carcinogenesis of CRC; **B** a network diagram of the oxidative stress-related gene APP signaling pathway, one of the signaling pathways of the cellular communication network, in which myofibroblasts communicate by sending and receiving signals from various cell populations. **C**, **D** Signaling pathway network diagram of the inflammatory response-related genes CD40 and LCK; **E**–**H** central score heatmap of the mononuclear/macrophage-related signaling pathway network, with the abscissa representing the cell subgroup and the ordinate representing the signaling roles in the communication network

in the TNF signaling network (Fig. 4E), according to the network center score heatmap of related signaling pathways in monocytes and macrophages (Fig. 4H).

3.4 Disturbance in the expression of oxidative stress and inflammatory response factors in a TCGA cohort

The TCGA-CRC cohort was first subjected to differential expression analysis. In all, 1795 differentially expressed genes were found using the volcano plot, comprising 806 upregulated genes and 989 downregulated genes, with 63 of these genes being associated with oxidative stress (Supplementary Fig. 1A). The heatmaps of their differential oxidative stress-related gene expression show that 24 of these genes were elevated in tumor samples, whereas 39 of these genes were downregulated (Supplementary Fig. 1B). a Heatmap showing the differential expression of 42 inflammatory response components, 25 of which were elevated in CRC (Supplementary Fig. 1C). The Venn diagram of all differentially expressed genes, genes associated with oxidative stress, and genes associated with the inflammatory response is shown, and it emphasizes MET and MMP14 as the common genes among the three groups (Supplementary Fig. 1D).

3.5 The potential of monocytes and macrophages to recognize tumor molecular subtypes

On the basis of single-cell data analysis, we found that monocytes and macrophages were more abundant and expressed oxidative stress and inflammatory response-related genes in CRC single cells. The most important and positively linked factors were their oxidative stress and inflammatory response. Additionally, the different oxidative stress and inflammatory responses between tumor and normal tissue cells were greatly influenced by monocytes and macrophages. Therefore, using marker genes for oxidative stress and the inflammatory response in monocytes and macrophages, we

attempted to classify molecular subtypes of CRC. Supplementary Fig. 2A–D depicts the clustering results, where K = 3 yields the best results. The distance is Euclidean, and the clustering procedure is km. The results of the sample clustering are shown in Table S4. The variation in the CDF curve's area under the curve when k is compared to k−1 (Supplementary Fig. 2E). Supplementary Fig. 2F, which depicts the cumulative distribution function when k takes different values, shows the consistent clustering cumulative distribution function (CDF), which demonstrates the cumulative distribution function. Additionally, we reduced the dimensions of the data using PCA principal component analysis and the t-distributed stochastic neighbor embedding (TSNE) algorithm, and we created a two-dimensional scatter diagram to confirm the accuracy of the clustering results (Supplementary Fig. 2G and H). The sample borders of the three subtypes are visible in both dimensionality reduction approaches, indicating successful clustering. When k = 2/3/4/5, we finally plotted KM curves between subtypes, and the results are shown in Supplementary Fig. 2 I–L. When K = 3, the results show that there is a discernible difference in subtype survival, with C2 showing the lowest survival. Since K = 3 had the best clustering effect and the most distinct survival curves among the subtypes, we chose it as the outcome of this molecular subtype recognition.

3.6 Differences in immune microenvironment between subtypes

To study differences in the immune milieu between subtypes, we analysed the function and proportion of immune infiltrating cells among subtypes based on the results of the molecular subtype recognition. Initially, we contrasted how oxidative stress and the inflammatory response varied among subtypes (Supplementary Fig. 3A–D). The C2 subtype had much higher enrichment scores for the gene sets associated with oxidative stress and the inflammatory response than the other two subtypes. The number of immune infiltrating cells in tumor samples was then calculated using the ESTIMATE algorithm, and differences between molecular subtypes were shown on a box plot using the matrix score, immune score, ESTIMATE score, and tumor purity (Supplementary Fig. 3E–H). The image makes it clear that the C2 subtype has significantly higher matrix, immune, and estimation scores than the other two subtypes, while having a lower tumor purity. Additionally, we determined the variation in the infiltration ratio of 28 immune cells among the three subtypes using the ssGSEA algorithm. Significant differences existed between the infiltration ratios of the 25 different types of cells, with the immune cell infiltration level in the C2 subtype being noticeably larger than that in the other two subtypes (Supplementary Fig. 3I).

3.7 Gene expression differences between molecular subtypes

Next, we compared the variations in immune-related factor expression across subtypes. The findings demonstrated that both common immunological checkpoints and antitumour-related factors had significantly greater expression levels in the C2 subtype (Supplementary Fig. 4A and B). We identified the elevated genes of each molecular subtype compared to the other samples and acquired a total of 383 differentially expressed genes between subtypes to investigate the variations in additional biological functions across molecular subtypes. The oxidative stress and inflammatory response genes were associated with the differentially expressed genes between subtypes (Supplementary Fig. 4C). Functional enrichment analysis of KEGG and GOBP was carried out using these differentially expressed genes, and the top 10 pathways with notable enrichment results were chosen for display. The KEGG pathway enrichment findings are provided. In immune-related pathways, such as bacterial infection, the interaction of viral proteins with cytokines and cytokine receptors, the interaction of cytokines and cytokine receptors, and the intestinal immune network produced by IgA, the differentially expressed genes between subtypes were mainly enriched (Supplementary Fig. 4D). According to the findings of GOBP functional enrichment, differentially expressed genes were primarily enriched in biological processes, including cell chemotaxis, cell migration, and other associated biological processes (Supplementary Fig. 4E).

3.8 Construction of prognostic risk model

We first carried out a univariate Cox analysis of differentially expressed genes among TCGA molecular subtypes to examine the effects of oxidative stress and the inflammatory response on the prognosis of CRC. Figure 5A shows the Cox analysis forest diagram for nine genes that were found to be substantially associated with the prognosis of CRC through p 0.01 (Table S3: cox_res). We then randomly selected 7/10 of the CRC total set (n = 591) from TCGA as the training set (n = 413) based on these 9 genes. To eliminate redundant genes from the training set, we utilized the Lasso linear regression approach with a seed value of 1110 and selected eight prognosis-related signatures (Table S3: lasso_res) (Fig. 5B).

The Kaplan–Meier survival curve of the model gene in the entire TCGA set was then plotted using the median expression of each gene as the cut-off value for high and low grouping. Notably, there were significant differences in the KM curves of all the genes, with MMP3 and ITLN1 having high expression levels acting as protective factors and the other five genes having high expression levels acting as risk factors (Fig. 5C–I). The expression patterns of the ZNF385A and ADAM8 genes in a single-cell dataset also show that these genes are significantly overexpressed in monocytes and macrophages (Fig. 5J and K).

3.9 TCGA internal validation model prognostic effectiveness

To further assess the influence of the model scores generated by the seven signatures on the overall survival period of the training set, we first determined the risk score for each sample in the dataset using the formula risk score = ADAM 8 * 0.191 + ANGPTL4 * 0.14 + ZNF385A * 0.013 + GPX3 * 0.103 + AOC3 * − 0.005 + MMP3 * 0.109 + ITLN1 * − 0.089 and then used the training set's high-risk and low-risk group gene expression distributions shown on the model gene expression heatmap (Supplementary Fig. 5A). Then, to see how survival and score relate to one another, we created scatter plots of survival time, survival status, and sample risk scores. Additionally, to compare the prognosis variations between the high-risk and low-risk groups, we created a KM curve. The KM curve showed a significant difference in prognosis between the two groups (Supplementary Fig. 5D), and the high-risk group sample had a worse prognosis (Supplementary Figs. 5B and C). We plotted the ROC curve of the prognostic signature using the built-in risk model. The model score had good prediction efficacy for 1/3/5 years, as indicated by the AUC values of 0.666, 0.687, and 0.672 (Supplementary Fig. 5E).

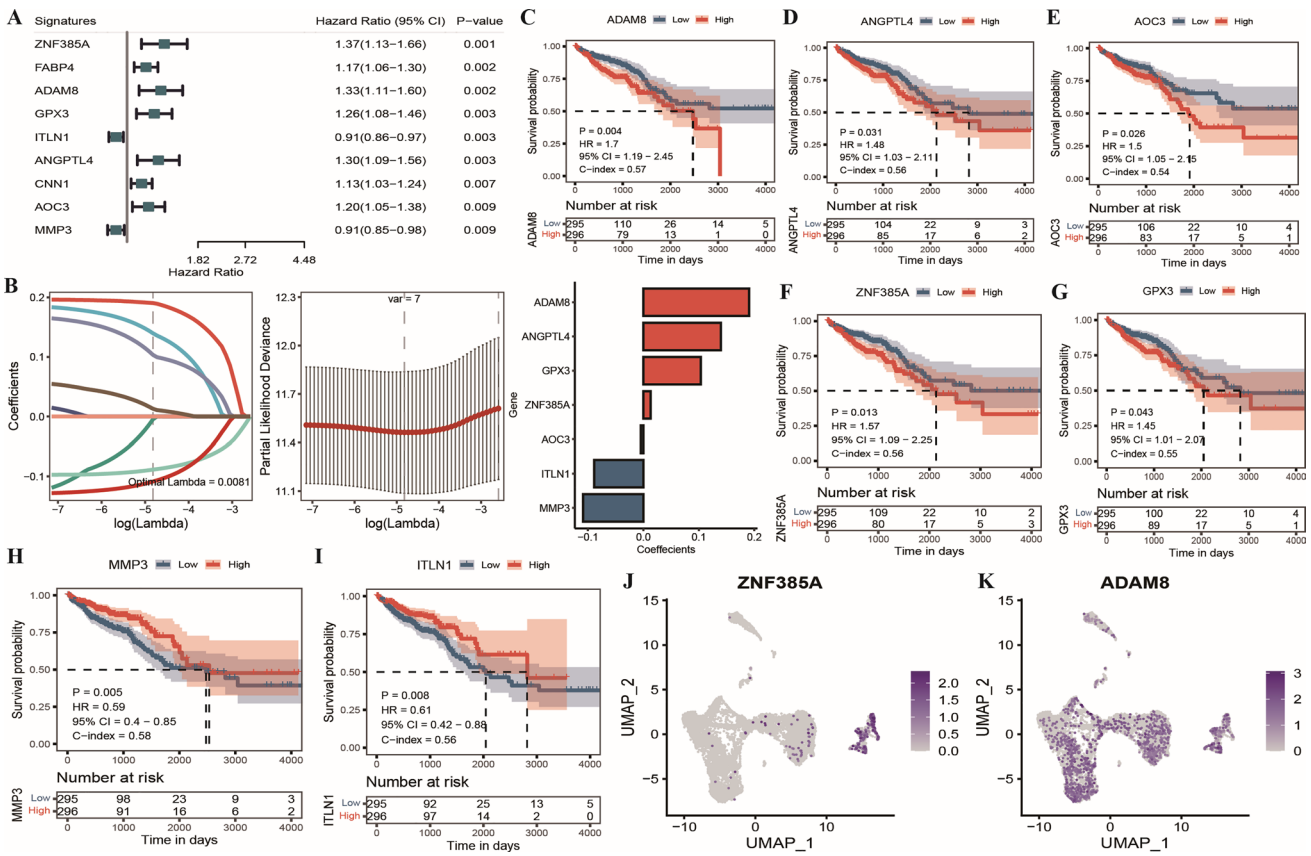

Fig. 5 **A** The Cox analysis forest diagram for nine genes that were found to be substantially associated with the prognosis of CRC. **B** We utilized the Lasso linear regression approach with a seed value of 1110 and selected eight prognostic-related signatures. **C–I** There are significant differences in the KM curves of all the genes, with MMP3 and ITLN1 having high expression levels acting as protective factors and the other five genes having high expression levels acting as risk factors. **J**, **K** The ZNF385A and ADAM8 genes in a single-cell dataset also show that these genes are significantly overexpressed in monocytes and macrophages

Then, we tested the capacity of the Riskscore to predict overall survival using the TCGA overall set of CRC (Supplementary Fig. 6). The model score shows strong and stable effectiveness in predicting survival, according to the TCGA ensemble's validation data.

We performed the same analysis using the external GEO datasets GSE161158 (Supplementary Fig. 7), GSE143985 (Supplementary Fig. 8), and GSE92921 (Supplementary Fig. 9) to further confirm the robustness of model scores in predicting overall survival in CRC patients. These findings show the model score's strong predictive power.

3.10 Risk scores are associated with multiple characteristics of CRC

To determine whether the RiskScore, when combined with data on stage, venous invasion, and lymphatic invasion, can be used as a standalone prognostic factor. There was both a single-factor and multiple-factor Cox regression analysis. The model risk score, age, and stage showed significant differences in single and multivariate Cox regression when other clinical variables were present, demonstrating their independence as prognostic factors (Fig. 6A). A nomogram that incorporated clinical markers of age and stage was later established based on survival time and survival status. The three variables were the most important clinical variables, with stage and risk score standing out among them (Fig. 6B). After that, the data on age, stage, groupings for venous invasion and lymphatic invasion, and cumulative distribution diagrams of high- and low-risk groups were examined. The findings showed a substantial correlation between the model grouping and the distribution of age, stage, venous invasion, and lymphatic invasion features (Fig. 6C–F). Finally, we looked at how the distribution of the risk score varied across different clinical feature groups. The risk score distribution showed a substantial difference depending on stage, venous invasion, and lymphatic invasion, proving that the clinical traits of CRC are linked to risk scores (Fig. 6G–I).

3.11 Functional differences between model groups

We examined the immune function differences between the high-risk and low-risk groups using the immune function gene pool enrichment score of CRC samples along with model grouping data. First, a heatmap was made to show the immune function gene set enrichment scores between the high- and low-risk groups (Supplementary Fig. 10A). Between the high- and low-risk groups, there were discernible differences in the enrichment scores of numerous immune function gene sets. The variations in HALLMARK gene pool enrichment scores between model groups were also contrasted. In contrast to oxidative phosphorylation and levels of cell death induced by oxidative stress, which were reduced in the high-risk group (Supplementary Fig. 10B–D), the interferon response rose in the high-risk group. The inflammatory response was also noticeably elevated in the high-risk group, according to Supplementary Fig. 10E.

3.12 Differences in immune microenvironment between model groups

We first evaluated the expression of 44 immunostimulatory checkpoints and 23 immunosuppressive checkpoints across high-risk and low-risk groups to examine the variations in immune checkpoint expression between model groups. The findings revealed substantial expression differences between the high-risk and low-risk groups for 10 immunosuppressive checkpoints and 23 immunostimulatory checkpoints (Supplementary Fig. 11A–B). Additionally, we contrasted variations in antitumour-related factors; the outcomes are shown in Supplementary Fig. 11C. Seven genes showed distinct expression patterns and were strongly expressed in the high-risk group, suggesting that their antitumour reactivity and immunity were improved.

We evaluated the differences in the proportion of infiltrating immune cells based on the estimated results of the proportion of infiltrating immune cells to investigate the differences in the tumor immune microenvironment between the high-risk and low-risk groups. a Box plot showing the differences in the four ESTIMATE algorithm scores between the high-risk and low-risk groups. The graph (Supplementary Fig. 11D) shows that the tumor purity of the high-risk group was lower than that of the low-risk group, while the tumor matrix, immunological, and estimation scores of the high-risk group were all noticeably higher than those of the low-risk group. A box plot of the variance in the proportion of 28 different types of infiltrating immune cells estimated using the ssGSEA method is also shown in Supplementary Fig. 11E. These showed notable differences in the infiltration proportion of 18 different immune cell types, and the proportion of macrophages was relatively low in the low-risk group.

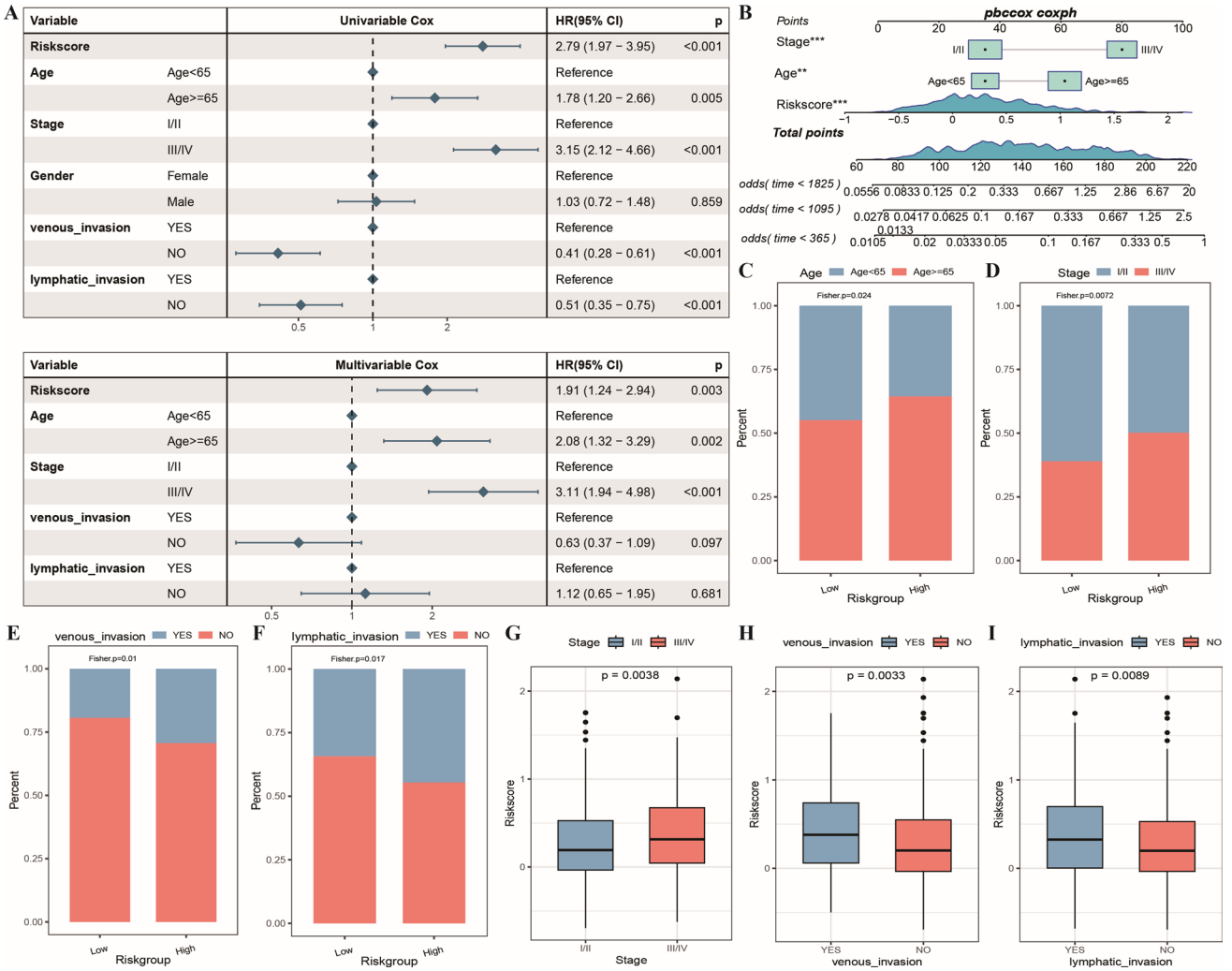

Fig. 6 **A** The model risk score, age, and stage show significant differences in single and multivariate Cox regression when other clinical variables are present, demonstrating their independence as prognostic factors. **B** The three variables were the most important clinical variables, with stage and risk score standing out among them. **C**–**F** The findings showed a substantial correlation between the model grouping and the distribution of age, stage, venous invasion, and lymphatic invasion features. **G**–**I** The risk score distribution showed a substantial difference depending on stage, venous invasion, and lymphatic invasion, proving that the clinical traits of CRC are linked to risk scores

3.13 Mutation differences between model groups

Gene alterations may support, encourage, or perpetuate cancerous spread. Therefore, understanding genomic mutations is important for creating new tumor therapies and targeted cancer medications. The TCGA_COAD and TCGA_READ cohorts' mutation information maf files were first combined, and then a waterfall graphic of the TOP30 gene mutation frequency was created by integrating model grouping with additional clinical data. The distribution of gene mutations in samples with various clinical features and high- and low-risk groups is shown. The genes with the highest frequency of mutation in CRC included APC, TP53, TTN, and KRAS (Supplementary Fig. 12A). Seven genes from the genes with CRC mutation frequency within TOP30 showed significant differences when we analysed the differences in gene mutation frequency between the high- and low-risk groups (Supplementary Fig. 12B). The sample was then split into MT and WT groups, and the difference in risk scores between the two groups was examined based on the status of these seven gene mutations. The results show that the risk scores of the wild-type group were significantly lower than those of the CCDC168, DNAH10, DNAH11, LRP2, and MUC16 mutant groups (Supplementary Fig. 12C–G).

3.14 Risk score predicts patient treatment effectiveness

We forecasted the IC50 values of 138 chemotherapeutic medications in the GDSC database using the expression profile of CRC in TCGA (Table S4: Drug_IC50). The IC50 values of 10 medications showed a substantial link with risk scores when we first assessed the correlation between risk scores and drug IC50 values. The first four medicines showed a substantial link with risk scores in a scatter plot that was created to show this (Supplementary Figs. 13A–D). The risk score and the IC50 of these medicines showed a negative connection.

We identified 84 medicines using statistical tests that had significantly different IC50 values between high- and low-risk groups based on model grouping findings and IC50 values. Their IC50 difference box charts were drawn in the high- and low-risk groups. For exhibition, five medications were chosen at random (Supplementary Fig. 13E–I). By examining the predictive power of tumor risk scores in patients' immunotherapy benefits, we further evaluated whether the model gene might be utilized as a marker for immunotherapy responses. We predicted the immunological response of samples in the TCGA CRC dataset using TIDE online analysis and then created a violin chart to show the distribution difference in risk scores between the reactive and nonreactive groups. The findings demonstrate that the risk score of the nonreactive group was significantly greater than that of the reactive group (Supplementary Fig. 13J). The cumulative distribution of reactive and nonreactive groups between high- and low-risk groups also differed significantly. In comparison to the high-risk group, the proportion of reactive samples in the low-risk group was noticeably higher (Supplementary Fig. 13K). Finally, we compared the IPS scores between the high- and low-risk groups in four categories (ips_ctla4_neg_pd1uneg, ips_ctla4_pos_pd1uneg, ips_ctla4_neg_pd1_pos, and ips_ctla4_pos_pd1_pos). Supplementary Fig. 13 L–N show the results, with the three IPS scores in the low-risk group being significantly higher than those in the high-risk group. Therefore, immunotherapy was more likely to be beneficial for patients in the low-risk group.

3.15 The expression of signature genes in unreported model genes ZNF385A in CRC

To verify the expression of the unreported model gene ZNF385A in CRC tissue, 10 CRC tissue specimens were tested. The results of the qPCR and IHC studies (Fig. 7A and B) revealed that the CRC tissues had a high level of ZNF385A expression. Next, Western blot experiments were performed to further explain the expression of ZNF385A in CRC. The results showed that ZNF385A was highly expressed in CRC tissue samples (Fig. 7C). To clarify the expression of unreported model genes in CRC cells, we used qPCR to analyse the expression of ZNF385A in CRC cells and found that ZNF385A was relatively highly expressed in SW620 and SW480 cells (Fig. 7D). To gain insights into the function of ZNF385A, we characterized the oncogenic phenotypes in SW620 cells with ZNF385A silencing (Si-ZNF385A-1 and Si-ZNF385A-2) and SW480 cells with ZNF385A overexpression (ZNF385A). The qPCR results showed that si-ZNF385A-1 and Si-ZNF385A-2 could significantly inhibit ZNF385A expression in CRC cells (SW620 cells) (Fig. 7E), and we chose Si-ZNF385A-1 and Si-ZNF385A-2 for cell function experiments. ZNF385A overexpression significantly upregulated ZNF385A expression in CRC cells (SW480 cells) (Fig. 7F).

3.16 Functional analysis of the unreported model gene ZNF385A in CRC

Reactive oxygen species (ROS) assays were used to quantify the ROS content in CRC cells, colony formation and EDU assays were used to detect cell proliferation, Transwell assays were used to assess the ability of CRC cells to invade and migrate, and xenograft model tumor assays were used to assess the regulatory roles of hub model genes in vivo. The functional experiment results indicated that the inhibition of ZNF385A expression suppressed the proliferation (Fig. 8A), migration, and invasion (Fig. 8C) and promoted ROS (Fig. 8B) in SW620 cells in vitro and the growth of xenograft tumors in vivo (Fig. 8D). Additionally, overexpression of ZNF385A significantly promoted SW480 cell proliferation (Fig. 9A), migration (Fig. 9C), and invasion (Fig. 9D) and inhibited ROS (Fig. 9B).

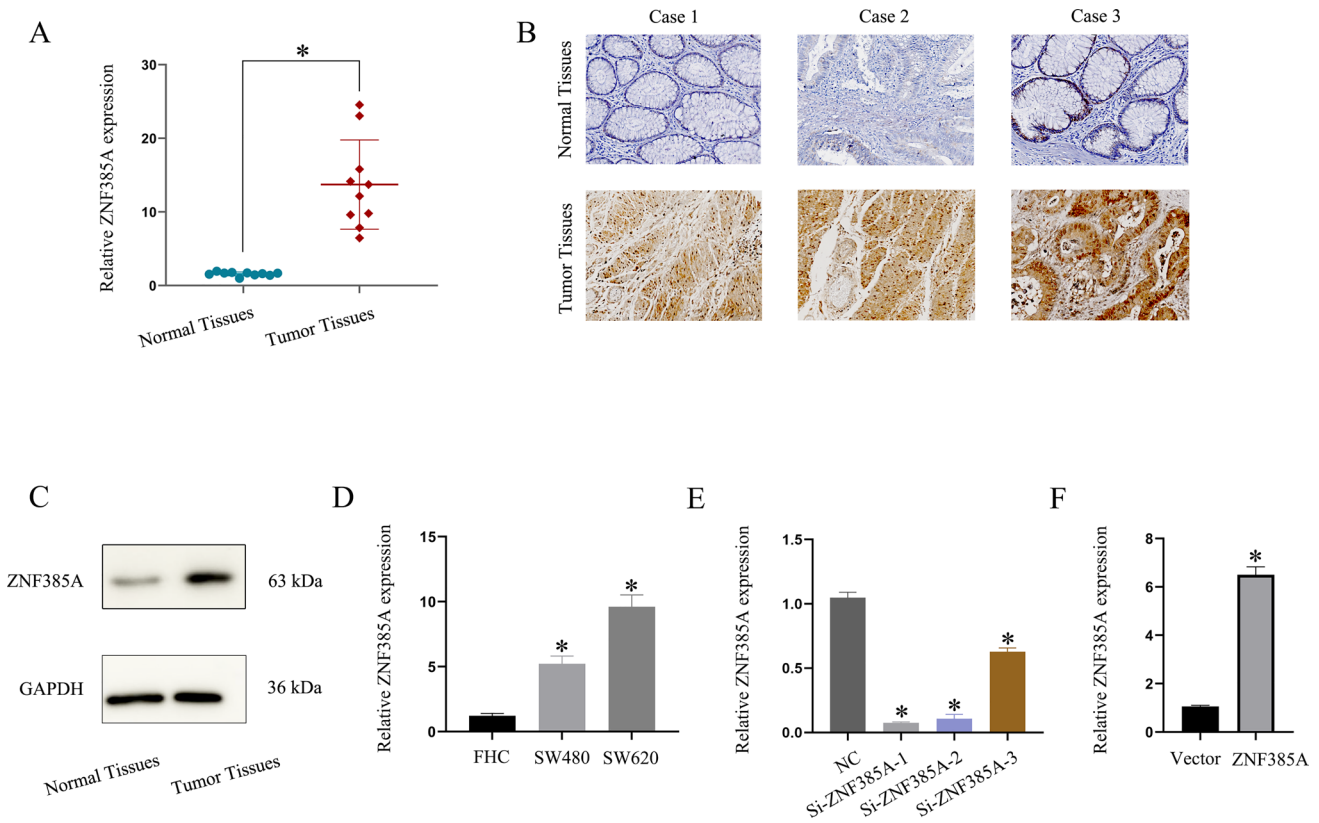

Fig. 7 Expression of the unreported model gene ZNF385A in CRC tissue. **A** and **B** The results of the qPCR and IHC studies revealed that CRC tissues had a high level of ZNF385A expression. **C** ZNF385A was highly expressed in CRC tissue samples. **D** ZNF385A was relatively highly expressed in SW620 and SW480 cells. **E** The qPCR results showed that si-ZNF385A-1 and si-ZNF385A-2 could significantly inhibit ZNF385A expression. **F** ZNF385A overexpression significantly upregulated ZNF385A expression

4 Discussion

The overall survival time of patients with advanced CRC has been improved by the new treatment regimen, but the survival rate of patients with metastatic CRC remains poor [18]. As CRC only presents symptoms in the late stage, it is crucial to improve early detection and reduce the incidence rate and mortality. In this study, a prognostic model for seven genes (ADAM8, ANGPTL4, ZNF385A, GPX3, AOC3, MMP3, and ITLN1) was constructed based on bioinformatics analysis and data from colorectal cancer patients in scRNASeq and TCGA cohorts. The clinical prognosis and correlation with tumor immunity were verified. Although some studies have reported prognostic models related to CRC [19–23], they only use data from a single database (TCGA), limiting the modelling accuracy. However, this study combined single-cell sequencing data, which makes the model more reliable. Furthermore, the prognostic model constructed in this study is based on newly discovered oxidative stress and inflammatory response genes, distinguishing it from other studies.

Excessive cellular oxidative stress is considered a significant factor in pathophysiological conditions and the development of cancer [24]. Normal cells utilize multiple mechanisms to maintain intracellular reactive oxygen species (ROS) levels and overall redox homeostasis to avoid damage to DNA, proteins, and lipids [25]. In contrast, cancer cells exhibit elevated ROS levels and upregulated protective antioxidant pathways [26]. The inflammatory response is a crucial component of the tumor microenvironment [27]. It is considered a physiological defense mechanism of the body against external stimuli such as cell damage and infection. During this process, the body releases many inflammatory mediators, such as cytokines and prostaglandins. However, long-term, uncontrolled inflammatory reactions may result in cell mutation and damage, leading to the occurrence of tumors [28]. Chronic inflammation caused by persistent infections due to microorganisms, viruses, worms, or sustained exposure to noninfectious factors such as smoke, silica, or asbestos may ultimately lead to carcinogenic effects [29]. This study developed a combination

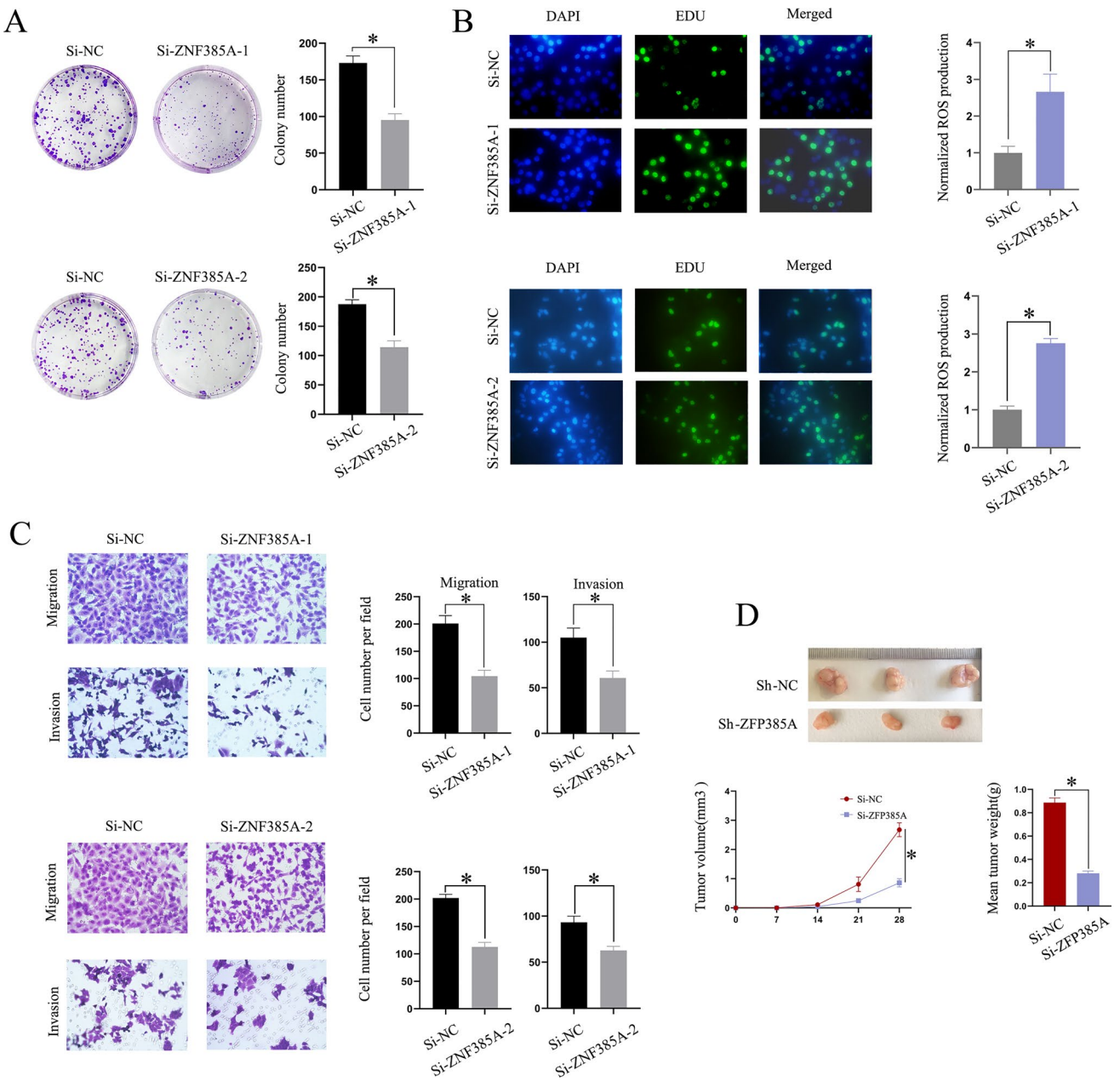

Fig. 8 The functional experiment results indicated that **A** the inhibition of ZNF385A expression suppressed proliferation, **B** promoted ROS, **C** suppressed the migration and invasion of SW620 cells in vitro and **D** suppressed the growth of xenograft tumors in vivo

of oxidative stress and inflammatory response scores for CRC to predict immunotherapy responses, further suggesting that our scores can be used to distinguish clinical patients and select more appropriate treatment options. Future research should prioritize the exploration of how ZNF385A interacts with specific oxidative stress markers and inflammatory mediators. This includes investigating its transcriptional regulation, post-translational modifications, and downstream signaling cascades. Moreover, it is crucial to determine how these interactions contribute to immune evasion or suppression, which are hallmarks of CRC progression. High-throughput sequencing technologies, along with advanced bioinformatics tools, could provide valuable insights into ZNF385A's role in orchestrating these complex biological processes.

In this study, we identified seven prognosis-related genes through mining, statistical analysis, and collation of TCGA, GEO, MsigDB, and GOBP datasets. Among these seven genes in CRC, GPX3 and AOC3 are important predictive genes related to oxidative stress in CRC, and they are associated with the pathogenesis of CRC [30, 31]. The

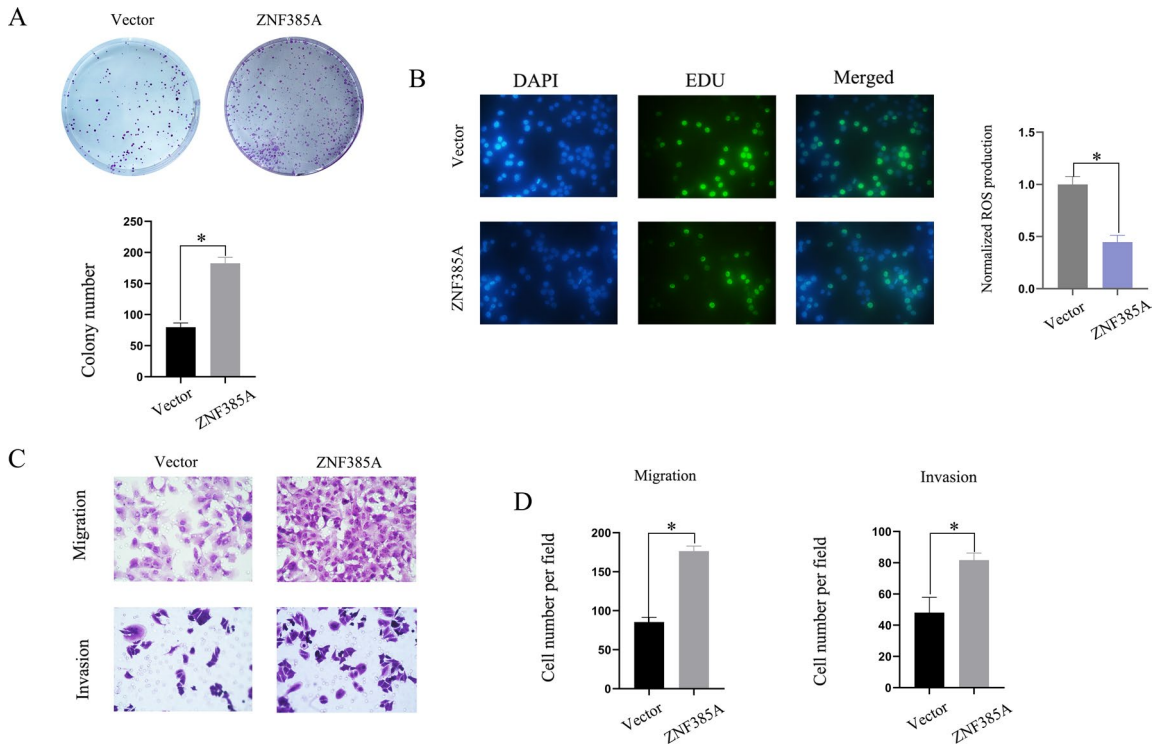

Fig. 9 The functional experiment results indicated that overexpression of ZNF385A significantly. **A** Promoted SW480 cell proliferation, **B** inhibit ROS. **C** and **D** promoted migration and invasion

downregulation of GPX3 can help CRC cells generate more energy under hypoxic conditions through a mechanism different from the "Warburg effect" [30]. AOC3 has been shown to promote tumor neovascularization, suggesting its involvement in tumorigenesis and progression [30]. ADAM8, ANGPTL1, MMP3, and ITLN1 are important predictive genes associated with inflammation in CRC [32–35]. Some studies have shown that ADAM8 can induce epithelial-mesenchymal transformation through the TGF-β/Smad2/3 signaling pathway, promoting the invasion of CRC cells [36]. ANGPTL1 attenuates cancer migration, invasion, and dryness by regulating FOXO3a-mediated SOX2 expression in CRC [37]. Histone deacetylase (HDAC11) inhibits the metastasis of CRC by suppressing the expression of matrix metalloproteinases (MMP3) [38]. ITLN1 can inhibit neovascularization and myelogenous inhibitory cell accumulation in CRC and may become a key prognostic and therapeutic target for CRC [39]. ZNF385A has recently emerged as a gene of interest in colorectal cancer (CRC) research due to its potential role as a novel oncogene. Despite no prior association between ZNF385A and CRC prognosis, our findings provide compelling evidence that it may serve as an important molecular marker and therapeutic target. Analysis of 10 CRC tissue specimens revealed significantly elevated expression levels of ZNF385A, confirmed through qPCR, IHC, and Western blot experiments. To elucidate its functional role, we examined the oncogenic phenotypes of ZNF385A in CRC cell lines. Silencing ZNF385A in SW620 cells (Si-ZNF385A-1 and Si-ZNF385A-2) led to notable suppression of proliferation, migration, invasion, and enhanced ROS levels in vitro, as well as reduced growth of xenograft tumors in vivo. Conversely, overexpression of ZNF385A in SW480 cells enhanced proliferation, migration, invasion, and decreased ROS levels, highlighting its potential as a driver of tumor progression. As a regulatory protein with functions in nucleic acid binding and p53 binding, ZNF385A likely plays a critical role in transcriptional regulation and cellular signaling in CRC. These findings underline the significance of ZNF385A as an oncogene and a promising target for future diagnostic and therapeutic strategies in CRC, warranting further exploration to unravel its detailed molecular mechanisms and clinical applications.

Our research still has some limitations. First, the data analysed are from publicly available databases. To further confirm the accuracy of gene prognostic models related to oxidative stress and the inflammatory response in predicting CRC prognosis, more CRC tissues need to be verified experimentally. Moreover, the specific mechanisms underlying the genes related to oxidative stress and the inflammatory response have not been thoroughly explored and require further investigation.

5 Conclusion

This study explored oxidative stress and inflammatory reactions at the single-cell level in CRC, which may contribute to the prognosis and immunotherapy of CRC. Additionally, we discovered ZNF385A to be a novel oncogene in CRC. These findings imply that this model may be applied to assess prognostic risk and identify potential therapeutic targets for CRC patients.

Acknowledgements We would like to thank the TCGA and GEO databases for the availability of the data

Author contributions Authors' contributio Yaqi Guo, Shipeng Shang designed the current study, analysed, interpreted the data. Leilei Liang collected the data, Enrui Liu supervised the study. All the authors have read and approved the final version of the manuscript and agreed to be accountable for all aspects of the research in ensuring that the accuracy or integrity of any part of the work is appropriately investigated and resolved.

Funding None.

Data availability The datasets used or analysed during the current study are available from the corresponding author upon reasonable request.

Declarations

Ethics approval and consent to participate This study was approved by the Ethics Committee of the Affiliated Hospital of Qingdao University. Informed consent was obtained from all participants in the study. All methods were carried out in accordance with relevant guidelines and regulations for both animal and human study.

Consent for publication Not applicable.

Competing interests The authors declare no competing interests.

References

1. Siegel RL, Wagle NS, Cercek A, Smith RA, Jemal A. Colorectal cancer statistics. CA Cancer J Clin. 2023. https://doi.org/10.3322/caac.21772. (**published online ahead of print, 2023 Mar 1**).
2. Benson AB, Venook AP, Al-Hawary MM, et al. NCCN guidelines insights: rectal cancer, version 6.2020. J Natl Compr Canc Netw. 2020;18(7):806–15. https://doi.org/10.6004/jnccn.2020.0032.
3. Keller DS, Berho M, Perez RO, Wexner SD, Chand M. The multidisciplinary management of rectal cancer. Nat Rev Gastroenterol Hepatol. 2020;17(7):414–29. https://doi.org/10.1038/s41575-020-0275-y.
4. Hawkins AT, Albutt K, Wise PE, et al. Abdominoperineal resection for rectal cancer in the twenty-first century: indications, techniques, and outcomes. J Gastrointest Surg. 2018;22(8):1477–87. https://doi.org/10.1007/s11605-018-3750-9.
5. Yang Y, Wang HY, Chen YK, Chen JJ, Song C, Gu J. Current status of surgical treatment of rectal cancer in China. Chin Med J (Engl). 2020;133(22):2703–11. https://doi.org/10.1097/CM9.0000000000001076.
6. Chen EY, Kardosh A, Nabavizadeh N, Lopez CD. Evolving treatment options and future directions for locally advanced rectal cancer. Clin Colorectal Cancer. 2019;18(4):231–7. https://doi.org/10.1016/j.clcc.2019.06.005.
7. Forman HJ, Zhang H. Targeting oxidative stress in disease: promise and limitations of antioxidant therapy. Nat Rev Drug Discov. 2021;20(9):689–709. https://doi.org/10.1038/s41573-021-00233-1. (**published correction appears in Nat Rev Drug Discov. 2021 Aug;20(8):652**).
8. Schmitt M, Greten FR. The inflammatory pathogenesis of colorectal cancer. Nat Rev Immunol. 2021;21(10):653–67. https://doi.org/10.1038/s41577-021-00534-x.
9. Srinivas US, Tan BWQ, Vellayappan BA, Jeyasekharan AD. ROS and the DNA damage response in cancer. Redox Biol. 2019;25: 101084. https://doi.org/10.1016/j.redox.2018.101084.
10. Patel M, Horgan PG, McMillan DC, Edwards J. NF-κB pathways in the development and progression of colorectal cancer. Transl Res. 2018;197:43–56. https://doi.org/10.1016/j.trsl.2018.02.002.
11. Lin Y, Jiang M, Chen W, Zhao T, Wei Y. Cancer and ER stress: mutual crosstalk between autophagy, oxidative stress and inflammatory response. Biomed Pharmacother. 2019;118: 109249. https://doi.org/10.1016/j.biopha.2019.109249.

12. Biasizzo M, Kopitar-Jerala N. Interplay between NLRP3 inflammasome and autophagy. Front Immunol. 2020;11: 591803. https://doi.org/10.3389/fimmu.2020.591803. (**Published 2020 Oct 9**).
13. Deng R, Zhang HL, Huang JH, et al. MAPK1/3 kinase-dependent ULK1 degradation attenuates mitophagy and promotes breast cancer bone metastasis. Autophagy. 2021;17(10):3011–29. https://doi.org/10.1080/15548627.2020.1850609.
14. Lei X, Lei Y, Li JK, et al. Immune cells within the tumor microenvironment: Biological functions and roles in cancer immunotherapy. Cancer Lett. 2020;470:126–33. https://doi.org/10.1016/j.canlet.2019.11.009.
15. Kuo CL, Ponneri Babuharisankar A, Lin YC, et al. Mitochondrial oxidative stress in the tumor microenvironment and cancer immunoescape: foe or friend? J Biomed Sci. 2022;29(1):74. https://doi.org/10.1186/s12929-022-00859-2. (**Published 2022 Sep 26**).
16. Kasprzak A. The role of tumor microenvironment cells in colorectal cancer (CRC) cachexia. Int J Mol Sci. 2021;22(4):1565. https://doi.org/10.3390/ijms22041565. (**Published 2021 Feb 4**).
17. Zeng D, Fang Y, Qiu W, Luo P, Wang S, Shen R, Gu W, Huang X, Mao Q, Wang G, Lai Y, Rong G, Xu X, Shi M, Wu Z, Yu G, Liao W. Enhancing immuno-oncology investigations through multidimensional decoding of tumor microenvironment with IOBR 20. Cell Rep Methods. 2024;4(12): 100910. https://doi.org/10.1016/j.crmeth.2024.100910.
18. Dekker E, Tanis PJ, Vleugels JLA, Kasi PM, Wallace MB. Colorectal cancer. Lancet. 2019;394(10207):1467–80. https://doi.org/10.1016/S0140-6736(19)32319-0.
19. Yue T, Chen S, Zhu J, et al. The aging-related risk signature in colorectal cancer. Aging (Albany NY). 2021;13(5):7330–49. https://doi.org/10.18632/aging.202589.
20. Wang J, Yu S, Chen G, et al. A novel prognostic signature of immune-related genes for patients with colorectal cancer. J Cell Mol Med. 2020;24(15):8491–504. https://doi.org/10.1111/jcmm.15443.
21. Liu S, Cao Q, An G, Yan B, Lei L. Identification of the 3-lncRNA signature as a prognostic biomarker for colorectal cancer. Int J Mol Sci. 2020;21(24):9359. https://doi.org/10.3390/ijms21249359. (**Published 2020 Dec 8**).
22. Ahluwalia P, Mondal AK, Bloomer C, et al. Identification and clinical validation of a novel 4 gene-signature with prognostic utility in colorectal cancer. Int J Mol Sci. 2019;20(15):3818. https://doi.org/10.3390/ijms20153818. (**Published 2019 Aug 5**).
23. Li M, Wang H, Li W, et al. Identification and validation of an immune prognostic signature in colorectal cancer. Int Immunopharmacol. 2020;88: 106868. https://doi.org/10.1016/j.intimp.2020.106868.
24. Azmanova M, Pitto-Barry A. Oxidative stress in cancer therapy: friend or enemy? ChemBioChem. 2022;23(10): e202100641. https://doi.org/10.1002/cbic.202100641.
25. Go YM, Jones DP. Redox compartmentalization in eukaryotic cells. Biochim Biophys Acta. 2008;1780(11):1273–90. https://doi.org/10.1016/j.bbagen.2008.01.011.
26. Cairns RA, Harris IS, Mak TW. Regulation of cancer cell metabolism. Nat Rev Cancer. 2011;11(2):85–95. https://doi.org/10.1038/nrc2981.
27. Khandia R, Munjal A. Interplay between inflammation and cancer. Adv Protein Chem Struct Biol. 2020;119:199–245. https://doi.org/10.1016/bs.apcsb.2019.09.004.
28. Greten FR, Grivennikov SI. Inflammation and cancer: triggers, mechanisms, and consequences. Immunity. 2019;51(1):27–41.
29. Masrour-Roudsari J, Ebrahimpour S. Causal role of infectious agents in cancer: an overview. Caspian J Internal Med. 2017;8(3):153–8. https://doi.org/10.22088/cjim.8.3.153.
30. Piran M, Sepahi N, Moattari A, Rahimi A, Ghanbariasad A. Systems biomedicine of primary and metastatic colorectal cancer reveals potential therapeutic targets. Front Oncol. 2021;11: 597536. https://doi.org/10.3389/fonc.2021.597536.
31. Danielli M, Thomas RC, Quinn LM, Tan BK. Vascular adhesion protein-1 (VAP-1) in vascular inflammatory diseases. Vasa. 2022;51(6):341–50. https://doi.org/10.1024/0301-1526/a001031.
32. Park GB, Choi S, Yoon YS, Kim D. TrkB/C-induced HOXC6 activation enhances the ADAM8-mediated metastasis of chemoresistant colon cancer cells. Mol Med Rep. 2021;23(6):423. https://doi.org/10.3892/mmr.2021.12062.
33. Sun R, Yang L, Hu Y, et al. ANGPTL1 is a potential biomarker for differentiated thyroid cancer diagnosis and recurrence. Oncol Lett. 2020;20(5):240. https://doi.org/10.3892/ol.2020.12103.
34. Kamal Y, Schmit SL, Hoehn HJ, Amos CI, Frost HR. Transcriptomic differences between primary colorectal adenocarcinomas and distant metastases reveal metastatic colorectal cancer subtypes. Cancer Res. 2019;79(16):4227–41. https://doi.org/10.1158/0008-5472.CAN-18-3945.
35. Katsuya N, Sentani K, Sekino Y, et al. Clinicopathological significance of intelectin-1 in colorectal cancer: intelectin-1 participates in tumor suppression and favorable progress. Pathol Int. 2020;70(12):943–52. https://doi.org/10.1111/pin.13027.
36. Jin Q, Jin X, Liu T, Lu X, Wang G, He N. A disintegrin and metalloproteinase 8 induced epithelial-mesenchymal transition to promote the invasion of colon cancer cells via TGF-β/Smad2/3 signalling pathway. J Cell Mol Med. 2020;24(22):13058–69. https://doi.org/10.1111/jcmm.15907.
37. Chang TY, Lan KC, Chiu CY, Sheu ML, Liu SH. ANGPTL1 attenuates cancer migration, invasion, and stemness through regulating FOXO3a-mediated SOX2 expression in colorectal cancer. Clin Sci (Lond). 2022;136(9):657–73. https://doi.org/10.1042/CS20220043.
38. Wen Y, Zhang X, Li X, et al. Histone deacetylase (HDAC) 11 inhibits matrix metalloproteinase (MMP) 3 expression to suppress colorectal cancer metastasis. J Cancer. 2022;13(6):1923–32. https://doi.org/10.7150/jca.66914. (**Published 2022 Mar 28**).
39. Chen L, Jin XH, Luo J, et al. ITLN1 inhibits tumor neovascularization and myeloid derived suppressor cells accumulation in colorectal carcinoma. Oncogene. 2021;40(40):5925–37. https://doi.org/10.1038/s41388-021-01965-5.